NANO LETTERS

pubs.acs.org/NanoLett Letter

Visualization and Manipulation of Bilayer Graphene Quantum Dots with Broken Rotational Symmetry and Nontrivial Topology

Zhehao Ge,[▽] Frederic Joucken,[▽] Eberth Quezada,[▽] Diego R. da Costa, John Davenport, Brian Giraldo, Takashi Taniguchi, Kenji Watanabe, Nobuhiko P. Kobayashi, Tony Low, and Jairo Velasco Jr.*

Cite This: https://dx.doi.org/10.1021/acs.nanolett.0c03453 Read Online

ACCESS | Metrics & More | Article Recommendations | Supporting Information

ABSTRACT: Electrostatically defined quantum dots (QDs) in Bernal stacked bilayer graphene (BLG) are a promising quantum information platform because of their long spin decoherence times, high sample quality, and tunability. Importantly, the shape of QD states determines the electron energy spectrum, the interactions between electrons, and the coupling of electrons to their environment, all of which are relevant for quantum information processing. Despite its importance, the shape of BLG QD states remains experimentally unexamined. Here we report direct visualization of BLG QD states by using a scanning tunneling microscope. Strikingly, we find these states exhibit a robust broken rotational symmetry. By using a numerical tight-binding model, we determine that the observed broken rotational symmetry can be attributed to low energy anisotropic bands. We then compare confined holes and electrons and demonstrate the influence of BLG's nontrivial band topology. Our study distinguishes BLG QDs from prior QD platforms with trivial band topology.

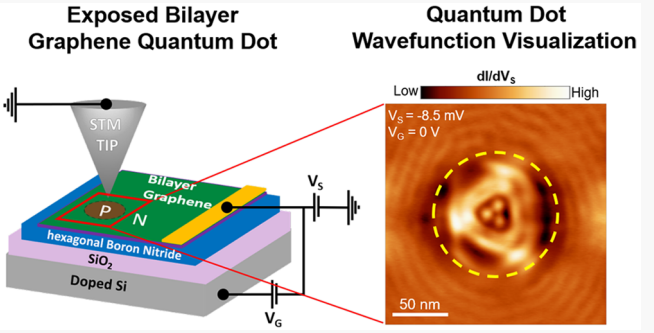

KEYWORDS: *quantum dots, bilayer graphene, Berry curvature, quantum information, scanning tunneling microscopy*

The visualization and manipulation of electronic states in quantum materials is of fundamental interest and has the potential for quantum information processing technologies.[1,2] Among the numerous quantum material platforms that are under consideration for these advanced technologies, Bernal stacked bilayer graphene (BLG) is highly attractive because it possesses an electric field tunable band gap.[3] This unique material property permits the realization of electrostatic quantum dots (QDs) with pristine boundaries and high flexibility to enable charge carrier confinement and QD state formation.[4,5] In addition, BLG QDs have long spin decoherence lifetimes,[6] controllable quantum degrees of freedom,[7,8] and nontrivial band topology.[9] These traits are all favorable for quantum information technology. Recent experimental progress with BLG QDs interfaced with sheets of hexagonal boron nitride (hBN) have demonstrated important advancements regarding quantum state control such as spin-valley resolved single electron charging[7,10] and magnetic field controlled valley splitting.[7,8] Of equal importance, is the understanding of the QD wave function shape, which determines the energy spectrum and allowable transitions between states. These energetics govern the preparation, manipulation, and readout of quantum information.[11] Theoretical predictions for BLG QD wave function shape are abundant;[12−16] however, the experimental validation of these predictions is lacking.

Here we use a scanning tunneling microscope (STM) tip to create an exposed circular p−n junction in a BLG/hBN heterostructure for imaging and manipulating new QD states. To create such nanostructures, we employed a tip voltage pulsing technique based on prior works with the formation of circular p−n junctions in graphene/hBN heterostructures[17,18] (see Supporting Information Section 1 for more information on tip pulsing technique). A schematized circular p−n junction and measurement setup is depicted in the left panel of Figure 1a. Our STM tip is grounded and a voltage bias (V_S) is applied to the sample. A gate voltage (V_G) is also applied to the underlying doped Si and is used to tune the BLG Fermi level.

To avoid the influence of adsorbates in our studies, we create circular p−n junctions in 200 × 200 nm^2 adsorbate free regions. The middle panel of Figure 1a shows the topography of one such region. The furthest right panel of Figure 1a shows an atomically resolved topography at the center of the region where a circular BLG p−n junction was created. Bright topographical features that form a triangular lattice are clearly

Received: August 26, 2020
Revised: November 14, 2020

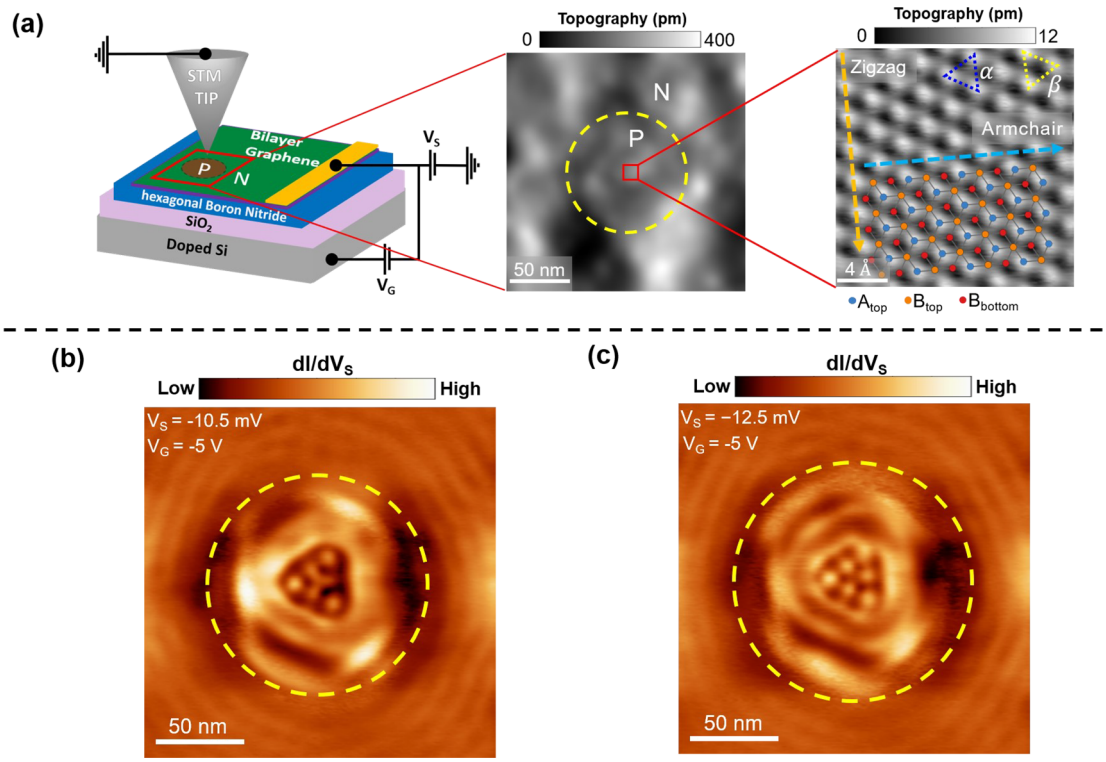

Figure 1. Scanning tunneling microscopy/spectroscopy (STM/STS) characterization of a circular bilayer graphene p−n junction. (a) Left panel: schematic of a STM tip probing a circular p−n junction in Bernal stacked bilayer graphene (BLG) that is supported by hexagonal boron nitride (hBN). The BLG/hBN heterostructure rests on a SiO_2/doped Si wafer.The STM tip is grounded, a sample bias V_S is applied between the BLG and ground, and a gate voltage V_G is applied between the doped Si and BLG. Middle panel: BLG topography after the creation of a circular p−n junction. Dashed yellow line denotes the p−n junction. The scanning parameters were $V_S = -8.5$ mV, $I = 0.3$ nA. Right panel: atomically resolved topography of BLG at the center of the p−n junction, the scanning parameters were $V_S = -100$ mV, $I = 2.5$ nA. BLG crystal structure is overlaid on the topography. The orange (blue) arrow indicates a BLG zigzag (armchair) direction(s). The blue and yellow triangles represent the two possible orientations for the BLG lattice by connecting the three closest bright atoms. (b, c) Constant sample bias dI/dV_S maps of circular BLG p−n junctions at $V_G = -5$ V (b, c). The yellow dashed line in (b) and (c) denotes the boundary between p and n doped regions. Scanning parameters for (b) and (c) are $V_{ac} = 2$ mV and $I = 0.3$ nA.

visible, as expected for BLG.[19,20] We overlay the atomic structure of BLG in this panel and use it to identify three of the four atoms within the BLG unit cell: A_{top}, B_{top}, and B_{bottom}. The fourth atom (A_{bottom}) on the bottom layer is obscured by B_{top}. In such a triangular lattice two orientations exist for the apparent triangles, we denote these orientations as α (dashed blue line that encloses B_{top}) and β (dashed yellow line that encloses B_{bottom}).

By performing constant sample bias dI/dV_S maps, we image the electronic states inside and outside of our circular BLG p−n junctions. In Figure 1b,c we show maps taken at two different energies $V_S = -10.5$ mV and $V_S = -12.5$ mV, but at the same $V_G = -5$ V. A dashed yellow line provides a guide to the eye for the p−n junction. The electronic states outside of the p−n junction exhibit an approximate circular symmetry consistent with the p−n junction shape itself. In contrast, the states within the p−n junction display a rich nodal pattern that breaks rotational symmetry. For example, in Figure 1b there is a "Y" shaped feature that can be seen at the center of the p−n junction with three antinodes that surround it. The pattern in Figure 1c, on the other hand, contains three distinct antinodes at the center of the junction. Despite the diverse nature of the patterns in each map, a clear C_3 symmetry is shared between both of them. Closer inspection of these electronic states also reveals that they are aligned with the orientation of the α triangle of the BLG lattice (see Supporting Information Section 4 for additional data on C_3 symmetry and BLG lattice alignment reproducibility).

To attain a more comprehensive understanding of the spatial distribution for the electronic states within our BLG p−n junctions, we acquired dI/dV_S spectra along zigzag and armchair directions across the center of the p−n junction from Figure 1b,c. The results of these measurements are shown in Figure 2a,b. The color scale corresponds to dI/dV_S amplitude and is plotted as a function of V_S and the distance across the circular p−n junction. These measurements were taken at $V_G = -5$ V. A distinct nodal level structure with high dI/dV_S amplitude is visible and is surrounded by a dark envelope (low dI/dV_S amplitude) in each of the two plots. Moreover, for the dI/dV_S spectra taken along the armchair direction (Figure 2a), the nodal distribution exhibits an asymmetric dI/dV_S intensity with respect to the center of the p−n junction. On the other hand, along the zigzag direction (Figure 2b), the nodal distribution of the same p−n junction exhibits a clear mirror symmetry with respect to the center of the junction. The well-defined difference seen between the armchair and zigzag directions indicates that the broken rotational symmetry observed in Figure 1b,c persists for a wide energy range.

Insight into the origin of our observations can be gained by considering the behavior of BLG charges corralled within a circular electrostatic potential well that is defined by a circular

https://dx.doi.org/10.1021/acs.nanolett.0c03453
Nano Lett. XXXX, XXX, XXX−XXX

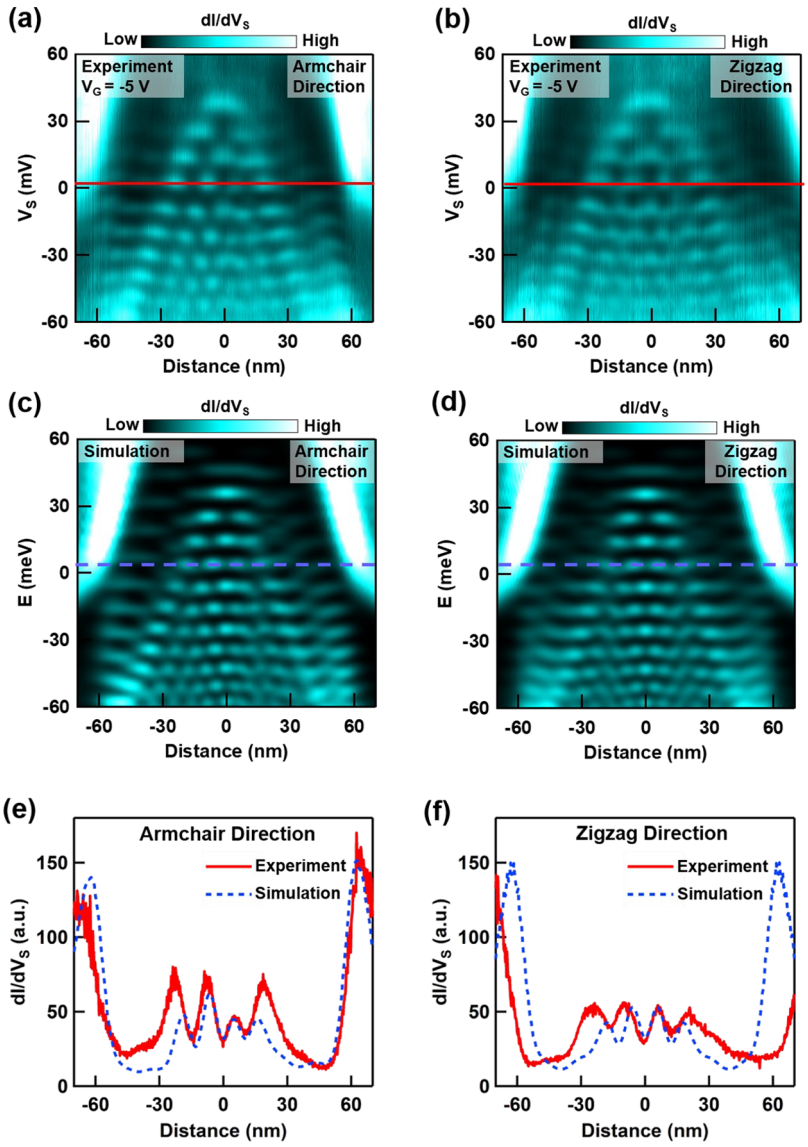

Figure 2. Spatially resolved energy levels inside a BLG quantum dot (QD) along zigzag and armchair directions. (a, b) Measured dI/dV_S spectra along BLG's armchair (a) and zigzag (b) directions at $V_G = -5$ V. The "0" on the horizontal axis in (a) and (b) denotes the center of the QD. The set point used in (a) and (b) was $I = 1$ nA, $V_S = -60$ mV, with a 2 mV ac modulation. (c, d) Simulated dI/dV_S spectra along the BLG armchair and zigzag direction, respectively. The "0" on the horizontal axis in (c) and (d) denotes the center of the QD in the TB model. A constant 60 meV gap (top layer was set at a higher energy than the bottom layer, $U = +60$ meV) and $\gamma_3 = -0.38$ eV were included in the model. (e) Comparison between experimental and simulated constant energy dI/dV_S profile along the BLG armchair direction. The experimental dI/dV_S profile was acquired from (a) at $V_S = 2$ mV, indicated by the red solid line. The simulated dI/dV_S profile was acquired from (c) at $E = 4$ meV, indicated by the blue dashed line. (f) Comparison between experiment and simulated constant energy dI/dV_S profile along zigzag direction. Theses profiles were acquired at the same energies as in (e).

p−n junction. This setup has extensive previous theoretical inquiry, yet as we will show, our experimental findings cannot be explained by these prior works. The touching BLG bands at the p−n junction are opened by the presence of a finite perpendicular electric field,[21,22] thus yielding charge carrier confinement and formation of QD states within the interior region of the circular p−n junction.[4,5,12,23] The dark envelope in Figure 2a,b indicates a reduction of electronic states at the p−n junction, hence revealing the presence of an electric field induced gap. Consequently, the nodal pattern enclosed by this electric field induced gap corresponds to the QD states in our experiment. The energetic and spatial distribution of these states are reminiscent of charges confined within a harmonic potential. For example, we find that the energy spacing of QD states that reside in the center is roughly uniform and approximately 24 meV. For BLG QDs, most theoretical investigations predicted circularly symmetric states[12−16] akin to QD states seen in monolayer graphene.[17,24] Notably, the C_3 symmetry that is clearly present in our QD states breaks rotational symmetry and is thus inconsistent with these prior predictions.

Interestingly, the electronic states within our QD exhibits the same symmetry as anisotropic low energy BLG bands that arise from the incorporation of a skewed interlayer hopping term γ_3.[25] This connection suggests an explanation for our findings and is also supported by a recent BLG QD theory that considered γ_3 hopping.[26] To verify this possibility, we proceeded by using numerical tight-binding (TB) calculations

https://dx.doi.org/10.1021/acs.nanolett.0c03453
Nano Lett. XXXX, XXX, XXX−XXX

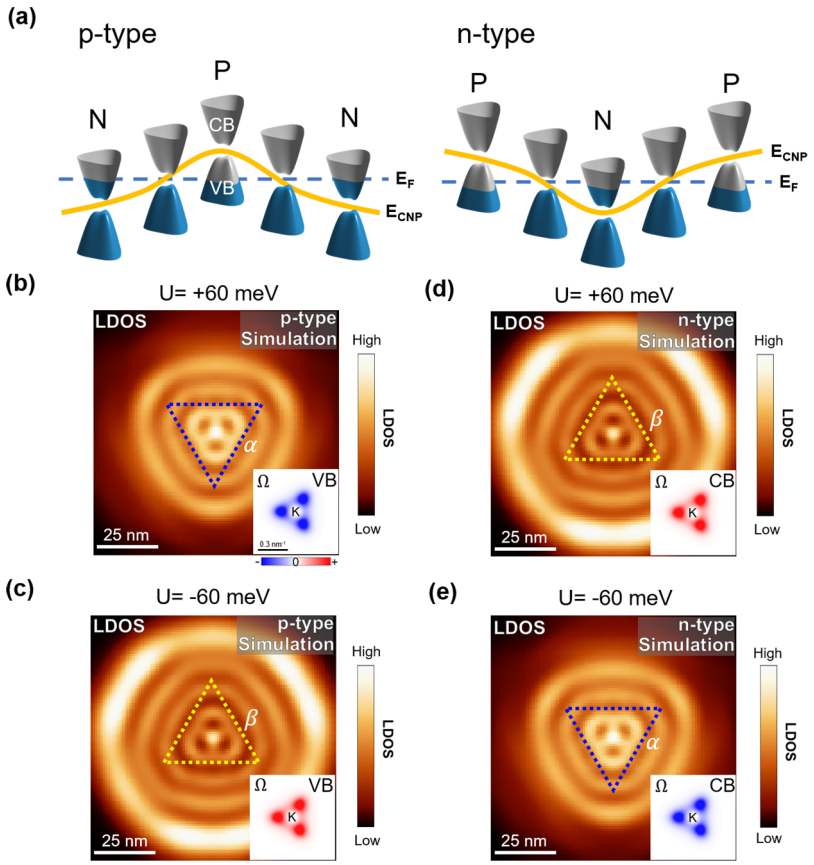

Figure 3. Simualted BLG QD LDOS tracks the Berry curvature sign switch. (a) Band diagrams for BLG QD with p-type (left panel) and n-type (right panel) central doping. The orange and blue curves indicate the BLG charge neutrality point (E_{CNP}) and Fermi level (E_F), respectively. BLG QDs with p-type and n-type central doping confine holes and electrons, respectively. (b)−(e) Simulated LDOS maps for a QD with p-type and n-type central doping. The potential well and the gap size is the same in (b, c), but the interlayer potential difference polarity (U) is +60 meV for (b) and (d) and −60 meV for (c) and (e). The blue triangle in (b) and (e) and yellow triangle in (c) and (d) represents the orientation of the α and β triangles of the BLG lattice in the TB model, respectively. Insets in (b, c) and (d, e) show the calculated Berry curvature (Ω) of the valence band (VB) and the conduction band (CB) near the K valley with U = +60 meV and U = −60 meV, respectively.

of a BLG QD that incorporates γ_3 hopping and a band gap. The potential well and the size of the band gap used in this calculation were extracted from the experiment (see Supporting Information Section 5 for details on the numerical calculation and model[27]). On the basis of this calculation, we simulated dI/dV_S spectra along BLG zigzag and armchair crystallographic directions that cross the center of the potential well. These simulations are shown in Figure 2c for the armchair direction and Figure 2d for the zigzag direction. Remarkably, the nodal distribution and dark envelope in the simulated dI/dV_S spectra closely resemble the measured spectra. For instance, the mirror symmetry about the center of the QD is clearly evident (absent) for the zigzag (armchair) direction(s). This symmetric (asymmetric) distribution of QD states along the zigzag (armchair) direction(s) can be attributed to the preservation (breaking) of mirror symmetry for BLG QDs along the zigzag (armchair) direction(s). The agreement between simulation and experiment is more apparent by comparing constant energy dI/dV_S profiles, as shown in Figure 2e,f. A strong agreement is also seen between experimental dI/dV_S maps and simulated constant energy local density of states (LDOS) maps (see Supplementary Section 6 for comparison). Crucially, we found that this agreement breaks down if either γ_3 or a band gap is excluded in the numerical TB calculation (see Supporting Information Section 7 for comparison).

The observed strong influence of gapped and anisotropic bands for BLG QD states has intriguing implications for accessing the nontrivial band topology of BLG. This is because such bands lead to a finite Berry curvature that is also anisotropic.[28] To explore this possible attribute of our QD system, we use simulations based on numerical TB calculations to study QDs with p-type and n-type central doping and with different interlayer potential difference polarities ($U > 0$ and $U < 0$). As shown in Figure 3a, the different types of QDs with gapped and anisotropic bands enable trapping of low energy holes (upper panel) and low energy electrons (lower panel). Simulated LDOS maps for analogous QDs with the same potential well curvature and gap size but with different polarity for the interlayer potential difference are shown in Figure 3b−e. First, we focus on QDs with p-type central doping (Figure 3b,c). We find that the orientation of the LDOS distribution for these QDs exhibits a 180° rotation between U = +60 meV and U = −60 meV. In addition, for U = +60 meV, the LDOS pattern is aligned with the α triangle of the BLG lattice, while for U = −60 meV the LDOS pattern is aligned with the β triangle of the BLG lattice. A similar rotation and LDOS pattern alignment with respect to the BLG lattice can also be seen for QDs with n-type central doping (Figure 3d,e).

https://dx.doi.org/10.1021/acs.nanolett.0c03453
Nano Lett. XXXX, XXX, XXX−XXX

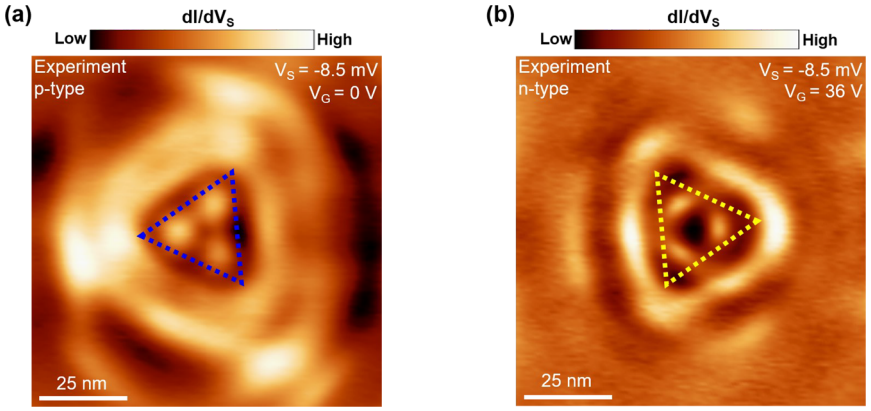

Figure 4. dI/dV_S maps reveal Berry curvature manipualtion within BLG QDs. (a) Measured constant energy dI/dV_S maps for a BLG QD with p-type central doping with scanning parameters I = 0.3 nA and V_{ac} = 2 mV. (b) Measured constant energy dI/dV_S maps for a BLG QD with n-type central doping with scanning parameters I = 0.1 nA and V_{ac} = 3 mV. The blue triangle in (a) and yellow triangle in (b) represent the orientations of α and β triangles of the BLG lattice, respectively.

The rotation in the simulated LDOS patterns indicates that a property of BLG has been modified between the different interlayer potential difference polarity configurations. The band structure of BLG does not depend on the interlayer potential difference polarity (see Supporting Information Section 9 for TB calculation of BLG band structure[25]). In contrast, the Berry curvature, which is related to the BLG band topology, does depend on the sign of the interlayer potential difference.[28−30] For example, for confined holes, the Berry curvature of BLG's valence band in the K valley is negative for U = +60 meV (see inset of Figure 3b). The Berry curvature of the same band is positive for U = −60 meV (see inset of Figure 3c). A similar Berry curvature sign flip can be seen for QDs with n-type central doping as well (insets of Figure 3d,e). Here we focus on one valley because the Berry curvature sign flip also occurs in the other valley when the interlayer potential polarity changes. Additionally, because time reversal symmetry is preserved in our BLG QDs, we expect that the two valleys remain degenerate and have the same LDOS distribution. The LDOS distribution can also be explained by considering that the Berry curvature sign and Fermi surface orientation are reversed in the two valleys (see Supporting Information Section 10 for further discussion). Thus, the simulated LDOS patterns in Figure 3b−e suggest that imaging the states within BLG QDs can reveal Berry curvature manipulation.

To experimentally verify this intriguing possibility, we created a circular p−n junction in the same region as the previous junctions but with different central doping types. We used this approach because in our experiment we were unable to modify the polarity of the interlayer potential difference (see Supporting Information Section 11 for additional details on interlayer potential difference[22]). Nonetheless, our simulations in Figure 3b,d reveal a 180° rotation between trapped holes and electrons. In addition, the LDOS pattern for trapped holes (electrons) is aligned with the α (β) triangle of the BLG lattice. These predictions from the simulations are consistent with the Berry curvature sign flip for the corresponding bands shown in the insets of Figure 3b,d.[28−30] Notably, panels a and b of Figure 4 show the measured dI/dV_S maps for QDs with p-type and n-type central doping, respectively. In exact agreement with the simulations, the orientations of the dI/dV_S patterns differ by a 180° rotation and they align with the α triangle of the BLG lattice for trapped holes and with the β triangle of the BLG lattice for trapped electrons.

In conclusion, we have spatially mapped BLG QD wave functions and demonstrated manipulation of their Berry curvature. We found that consideration of gapped and anisotropic low energy bands is crucial for understanding the behavior of electrostatically corralled BLG charges. Additionally, we revealed manifestations of the nontrivial BLG band topology by imaging the quantum interference in our BLG QDs. This finding could inspire future works using quantum interference to study the properties of materials that have finite Berry curvature such as semiconducting transition metal dichalcogenides[31] (e.g., MoS_2), topological insulators[32] (e.g., WTe_2), and Weyl semimetals[33−35] (e.g., TaAs). The technical advancements presented here can also be used to study more sophisticated platforms for quantum information technology such as BLG double and multiple QDs. The tunable couplings in these systems make them promising for the realization of quantum bits based on spin and valley degrees of freedom.[36,37]

■ ASSOCIATED CONTENT

Supporting Information

The Supporting Information is available free of charge at https://pubs.acs.org/doi/10.1021/acs.nanolett.0c03453.

(1) Description of tip pulsing procedure, (2) sample fabrication, STM measurements, and tip cleaning, (3) circular symmetry of BLG QD, (4) reproducibility of BLG QD states, (5) numerical tight-binding calculations, (6) comparison between experimental dI/V_S maps and simulated LDOS maps, (7) discussion on the importance of γ_3, (8) evaluation of BLG QD state symmetry along different crystallographic directions, (9) BLG band structure with two different interlayer potential polarities, (10) heuristic for predicting orientation of real space LDOS distribution of BLG QD, (11) determination of the interlayer potential difference, (12) QD wave function orientation on top and bottom layers of BLG, (13) determination of upper and lower bounds for γ_3 based on experiment and simulation comparison, (14) QD states probed with different gate and bias voltage combinations, (15) determination of QD lever arm; Figures S1−S19 showing STM and AFM images, schematic of hopping parameters, graphs, structures, band structures, and heuristic schematic (PDF)

https://dx.doi.org/10.1021/acs.nanolett.0c03453
Nano Lett. XXXX, XXX, XXX−XXX

AUTHOR INFORMATION

Corresponding Author

Jairo Velasco Jr. − *Department of Physics, University of California, Santa Cruz, California 95064, United States;* orcid.org/0000-0002-3493-1095; Email: jvelasc5@ucsc.edu

Authors

Zhehao Ge − *Department of Physics, University of California, Santa Cruz, California 95064, United States*

Frederic Joucken − *Department of Physics, University of California, Santa Cruz, California 95064, United States;* orcid.org/0000-0002-9056-0081

Eberth Quezada − *Department of Physics, University of California, Santa Cruz, California 95064, United States*

Diego R. da Costa − *Departamento de Física, Universidade Federal do Ceará, 60455-900 Fortaleza, Ceará, Brazil*

John Davenport − *Department of Physics, University of California, Santa Cruz, California 95064, United States*

Brian Giraldo − *Jack Baskin School of Engineering, University of California, Santa Cruz, California 95064, United States*

Takashi Taniguchi − *International Center for Materials Nanoarchitectronics, National Institute for Materials Science, Tsukuba 305-0044, Japan;* orcid.org/0000-0002-1467-3105

Kenji Watanabe − *Research Center for Functional Materials, National Institute for Materials Science, Tsukuba 305-0044, Japan;* orcid.org/0000-0003-3701-8119

Nobuhiko P. Kobayashi − *Jack Baskin School of Engineering, University of California, Santa Cruz, California 95064, United States;* orcid.org/0000-0002-2721-1057

Tony Low − *Department of Electrical and Computer Engineering, University of Minnesota, Minneapolis, Minnesota 55455, United States;* orcid.org/0000-0002-5759-5899

Complete contact information is available at: https://pubs.acs.org/10.1021/acs.nanolett.0c03453

Author Contributions

[▽]Z.G., F.J., and E.Q. contributed equally to this manuscript.

Author Contributions

J.V.J., Z.G., F.J., and E.Q. conceived the work and designed the research strategy. Z.G. and F.J. performed data analysis under J.V.J.'s supervision. Z.G., E.Q., J.D., and B.G. fabricated the samples under N.P.K. and J.V.J.'s supervision. K.W. and T.T. provided the hBN crystals. Z.G., F.J., and E.Q. carried out tunneling spectroscopy measurements under J.V.J.'s supervision. Z.G. performed numerical TB calculations and simulations with input from D.R.C. and T.L. D.R.C. performed additional calculations under T.L.'s supervision. Z.G., F.J., and J.V.J. developed interpretation for experimental findings with input from D.R.C. and T.L. J.V.J., Z.G., and F.J. wrote the paper. All authors discussed the paper and commented on the manuscript.

Funding

J.V.J. acknowledges support from the National Science Foundation under award DMR-1753367 and the Army Research Office under contract W911NF-17-1-0473. K.W. and T.T. acknowledge support from the Elemental Strategy Initiative conducted by the MEXT, Japan, Grant Number JPMXP0112101001, JSPS KAKENHI Grant Numbers JP20H00354 and the CREST(JPMJCR15F3), JST.

Notes

The authors declare no competing financial interest.

ACKNOWLEDGMENTS

We thank the Hummingbird Computational Cluster team at UC Santa Cruz for providing computational resources and support for the numerical TB calculations performed in this work.

REFERENCES

(1) Basov, D.; Averitt, R.; Hsieh, D. Towards properties on demand in quantum materials. *Nat. Mater.* **2017**, *16*, 1077−1088.

(2) Liu, X.; Hersam, M. C. 2D materials for quantum information science. *Nature Reviews Materials* **2019**, *4*, 669−684.

(3) Bockrath, M. Unprecedented Charge State Control in Graphene Quantum Dots. *Nano Lett.* **2020**, *20*, 2937−2938.

(4) Goossens, A. M.; Driessen, S. C.; Baart, T. A.; Watanabe, K.; Taniguchi, T.; Vandersypen, L. M. Gate-defined confinement in bilayer graphene-hexagonal boron nitride hybrid devices. *Nano Lett.* **2012**, *12*, 4656−4660.

(5) Allen, M. T.; Martin, J.; Yacoby, A. Gate-defined quantum confinement in suspended bilayer graphene. *Nat. Commun.* **2012**, *3*, 934.

(6) Trauzettel, B.; Bulaev, D. V.; Loss, D.; Burkard, G. Spin qubits in graphene quantum dots. *Nat. Phys.* **2007**, *3*, 192−196.

(7) Eich, M.; Pisoni, R.; Overweg, H.; Kurzmann, A.; Lee, Y.; Rickhaus, P.; Ihn, T.; Ensslin, K.; Herman, F.; Sigrist, M. Spin and Valley States in Gate-Defined Bilayer Graphene Quantum Dots. *Phys. Rev. X* **2018**, *8*, No. 031023.

(8) Kurzmann, A.; Eich, M.; Overweg, H.; Mangold, M.; Herman, F.; Rickhaus, P.; Pisoni, R.; Lee, Y.; Garreis, R.; Tong, C. Excited states in bilayer graphene quantum dots. *Phys. Rev. Lett.* **2019**, *123*, No. 026803.

(9) Lee, Y.; Knothe, A.; Overweg, H.; Eich, M.; Gold, C.; Kurzmann, A.; Klasovika, V.; Taniguchi, T.; Wantanabe, K.; Fal'ko, V. Tunable Valley Splitting due to Topological Orbital Magnetic Moment in Bilayer Graphene Quantum Point Contacts. *Phys. Rev. Lett.* **2020**, *124*, 126802.

(10) Velasco, J., Jr; Lee, J.; Wong, D.; Kahn, S.; Tsai, H.-Z.; Costello, J.; Umeda, T.; Taniguchi, T.; Watanabe, K.; Zettl, A. Visualization and Control of Single-Electron Charging in Bilayer Graphene Quantum Dots. *Nano Lett.* **2018**, *18*, 5104−5110.

(11) Yamamoto, Y., Semba, K., Eds. *Principles and Methods of Quantum Information Technologies*; Springer, 2016.

(12) Pereira, J. M.; Vasilopoulos, P.; Peeters, F. Tunable quantum dots in bilayer graphene. *Nano Lett.* **2007**, *7*, 946−949.

(13) Matulis, A.; Peeters, F. Quasibound states of quantum dots in single and bilayer graphene. *Phys. Rev. B: Condens. Matter Mater. Phys.* **2008**, *77*, 115423.

(14) Recher, P.; Nilsson, J.; Burkard, G.; Trauzettel, B. Bound states and magnetic field induced valley splitting in gate-tunable graphene quantum dots. *Phys. Rev. B: Condens. Matter Mater. Phys.* **2009**, *79*, No. 085407.

(15) Zarenia, M.; Partoens, B.; Chakraborty, T.; Peeters, F. Electron-electron interactions in bilayer graphene quantum dots. *Phys. Rev. B: Condens. Matter Mater. Phys.* **2013**, *88*, 245432.

(16) Hou, Z.; Zhou, Y.-F.; Xie, X.; Sun, Q.-F. Berry phase induced valley level crossing in bilayer graphene quantum dots. *Phys. Rev. B: Condens. Matter Mater. Phys.* **2019**, *99*, 125422.

(17) Lee, J.; Wong, D.; Velasco, J., Jr; Rodriguez-Nieva, J. F.; Kahn, S.; Tsai, H.-Z.; Taniguchi, T.; Watanabe, K.; Zettl, A.; Wang, F. Imaging electrostatically confined Dirac fermions in graphene quantum dots. *Nat. Phys.* **2016**, *12*, 1032.

(18) Velasco, J.; Ju, L.; Wong, D.; Kahn, S.; Lee, J.; Tsai, H.-Z.; Germany, C.; Wickenburg, S.; Lu, J.; Taniguchi, T.; Watanabe, K.; Zettl, A.; Wang, F.; Crommie, M. F. Nanoscale Control of Rewriteable Doping Patterns in Pristine Graphene/Boron Nitride Heterostructures. *Nano Lett.* **2016**, *16*, 1620−1625.

https://dx.doi.org/10.1021/acs.nanolett.0c03453
Nano Lett. XXXX, XXX, XXX−XXX

(19) Lauffer, P.; Emtsev, K.; Graupner, R.; Seyller, T.; Ley, L.; Reshanov, S.; Weber, H. Atomic and electronic structure of few-layer graphene on SiC (0001) studied with scanning tunneling microscopy and spectroscopy. *Phys. Rev. B: Condens. Matter Mater. Phys.* **2008**, *77*, 155426.
(20) Kim, K. S.; Kim, T.-H.; Walter, A. L.; Seyller, T.; Yeom, H. W.; Rotenberg, E.; Bostwick, A. Visualizing atomic-scale negative differential resistance in bilayer graphene. *Phys. Rev. Lett.* **2013**, *110*, No. 036804.
(21) McCann, E. Asymmetry gap in the electronic band structure of bilayer graphene. *Phys. Rev. B: Condens. Matter Mater. Phys.* **2006**, *74*, 161403.
(22) Zhang, Y.; Tang, T.-T.; Girit, C.; Hao, Z.; Martin, M. C.; Zettl, A.; Crommie, M. F.; Shen, Y. R.; Wang, F. Direct observation of a widely tunable bandgap in bilayer graphene. *Nature* **2009**, *459*, 820.
(23) Nandkishore, R.; Levitov, L. Common-path interference and oscillatory Zener tunneling in bilayer graphene pn junctions. *Proc. Natl. Acad. Sci. U. S. A.* **2011**, *108*, 14021−14025.
(24) Gutiérrez, C.; Brown, L.; Kim, C.-J.; Park, J.; Pasupathy, A. N. Klein tunnelling and electron trapping in nanometre-scale graphene quantum dots. *Nat. Phys.* **2016**, *12*, 1069−1075.
(25) McCann, E.; Koshino, M. The electronic properties of bilayer graphene. *Rep. Prog. Phys.* **2013**, *76*, No. 056503.
(26) Knothe, A.; Fal'ko, V. Quartet states in two-electron quantum dots in bilayer graphene. *Phys. Rev. B: Condens. Matter Mater. Phys.* **2020**, *101*, 235423.
(27) Moldovan, D.; Andelkovic, M.; Peeters, F. *pybinding v0.9.5: a Python package for tight-binding calculations*; Zendo, 2020, DOI: 10.5281/zenodo.4010216.
(28) Knothe, A.; Fal'ko, V. Influence of minivalleys and Berry curvature on electrostatically induced quantum wires in gapped bilayer graphene. *Phys. Rev. B: Condens. Matter Mater. Phys.* **2018**, *98*, 155435.
(29) Shimazaki, Y.; Yamamoto, M.; Borzenets, I. V.; Watanabe, K.; Taniguchi, T.; Tarucha, S. Generation and detection of pure valley current by electrically induced Berry curvature in bilayer graphene. *Nat. Phys.* **2015**, *11*, 1032.
(30) Xiao, D.; Chang, M.-C.; Niu, Q. Berry phase effects on electronic properties. *Rev. Mod. Phys.* **2010**, *82*, 1959.
(31) Mak, K. F.; McGill, K. L.; Park, J.; McEuen, P. L. The valley Hall effect in MoS2 transistors. *Science* **2014**, *344*, 1489−1492.
(32) Xu, S.-Y.; Ma, Q.; Shen, H.; Fatemi, V.; Wu, S.; Chang, T.-R.; Chang, G.; Valdivia, A. M. M.; Chan, C.-K.; Gibson, Q. D. Electrically switchable Berry curvature dipole in the monolayer topological insulator WTe 2. *Nat. Phys.* **2018**, *14*, 900−906.
(33) Weng, H.; Fang, C.; Fang, Z.; Bernevig, B. A.; Dai, X. Weyl semimetal phase in noncentrosymmetric transition-metal monophosphides. *Phys. Rev. X* **2015**, *5*, No. 011029.
(34) Xu, S.-Y.; Belopolski, I.; Alidoust, N.; Neupane, M.; Bian, G.; Zhang, C.; Sankar, R.; Chang, G.; Yuan, Z.; Lee, C.-C. Discovery of a Weyl fermion semimetal and topological Fermi arcs. *Science* **2015**, *349*, 613−617.
(35) Lv, B.; Weng, H.; Fu, B.; Wang, X.; Miao, H.; Ma, J.; Richard, P.; Huang, X.; Zhao, L.; Chen, G. Experimental discovery of Weyl semimetal TaAs. *Phys. Rev. X* **2015**, *5*, No. 031013.
(36) Eich, M.; Pisoni, R.; Pally, A.; Overweg, H.; Kurzmann, A.; Lee, Y.; Rickhaus, P.; Watanabe, K.; Taniguchi, T.; Ensslin, K. Coupled quantum dots in bilayer graphene. *Nano Lett.* **2018**, *18*, 5042−5048.
(37) Banszerus, L.; Möller, S.; Icking, E.; Watanabe, K.; Taniguchi, T.; Volk, C.; Stampfer, C. Single-electron double quantum dots in bilayer graphene. *Nano Lett.* **2020**, *20*, 2005−2011.

https://dx.doi.org/10.1021/acs.nanolett.0c03453
Nano Lett. XXXX, XXX, XXX−XXX